Electron loss and multiple electron capture of B^{2+} and C^{3+} ions colliding with Ne and Ar targets

W. Wolff, H. Luna, A. C. F. Santos, and E. C. Montenegro
Instituto de Física, Universidade Federal do Rio de Janeiro, Caixa Postal 68528, Rio de Janeiro 21945-970, RJ, Brazil

G. M. Sigaud*
Departamento de Física, Pontifícia Universidade Católica do Rio de Janeiro, Caixa Postal 38071, Rio de Janeiro 22452-970, RJ, Brazil
(Received 27 April 2009; published 3 September 2009)

Absolute cross sections for the projectile single-electron loss and single- and double-electron capture of B^{2+} ions colliding with Ne and Ar targets and C^{3+} ions colliding with Ar targets, in the energy range from 0.1 to 4.0 MeV, have been measured. Cross sections for the single capture channel have been calculated using the classical Bohr-Lindhard model, showing good agreement with the experiment. In the single electron-loss process, calculations were performed using both an extended version of the classical-impulse free-collision model and the plane-wave Born approximation (PWBA) for the screening mechanism, added to antiscreening cross sections calculated with the PWBA, thus providing total single electron-loss cross sections. The total cross sections obtained from the former method provided very good descriptions of the single electron-loss measured data, much better than those from the PWBA. The antiscreening calculations have been compared to experimental cross sections for ionization of B^{2+} and C^{3+} ions by electrons, within the independent-particle model, showing a good agreement in the asymptotic high-velocity region.

DOI: 10.1103/PhysRevA.80.032703 PACS number(s): 34.50.Fa, 52.20.Hv

I. INTRODUCTION

Charge-changing processes in ion-atom collisions with active electrons on both partners—such as projectile electron loss and electron capture—have been studied extensively for the past decades, since they are important in many fields of research as, for example, accelerator technology [1], plasma physics [2], and nuclear fusion, where these processes with dressed projectile ions can cause undesired beam transport losses and losses in storage rings [3,4]. From the more fundamental point of view, collisions between dressed ions and neutral atoms in the low-to-intermediate-velocity regime present several interesting issues of electron dynamics of few-body systems in a region where perturbative methods are not reliable, mainly when there are more than two active electrons in the system [5–7]. For this reason, the investigation of collisions between Li-like projectiles, with velocities ranging from below 1 to a few atomic units, and noble gas targets can provide useful information to increase our knowledge about charge-changing processes in a nonperturbative regime, since one can consider the 2*s* electron of these projectiles as the only active electron contributing to the projectile electron loss. Moreover, Li-like projectiles, such as B^{2+} and C^{3+}, are more efficient to the electron-capture process than, for example, H^+ or He^+ in this velocity range, due to their larger effective charge.

However, experimental absolute cross sections for electron loss and capture for these Li-like projectiles are rather scarce. The work from Melo *et al.* on collisions of C^{3+} and O^{5+} with noble gases in the intermediate-velocity range, where both absolute measurements and nonperturbative calculations of single and multiple electron loss and capture cross sections [5] were presented, and those from Dmitriev *et al.* for electron capture and loss absolute data on collisions of B ions with Ne and Ar targets at two projectile velocities, namely, 1.19 and 1.83 a.u [8], and of C ions with He, Ar, and N_2 targets in the same velocity region [9] are, to the authors' knowledge, the only absolute data existent in the literature. In the case of B ions, which are of special interest for the study of thermonuclear fusion plasmas, since they are among the most abundant impurities in fusion reactors (for a comprehensive review, see the papers published in Ref. [10]), the large majority of experimental and theoretical results are restricted to atomic and molecular H_2 and He targets [11–26].

In this paper, we present measurements of absolute cross sections for the single-electron loss and single- and double-electron capture for B^{2+} by Ne and Ar targets, and for C^{3+} by Ar targets, in the energy range from 0.1 to 4.0 MeV. The data obtained here were compared with the other available results for Li-like projectiles on the same targets. In the case of C^{3+}, we have extended the previous measurements of Melo *et al.* [5] and Dmitriev *et al.* [9] to lower velocities, thus reaching a less perturbative regime. For the B^{2+} projectile, besides providing a more comprehensive set of data than those presented by Dmitriev *et al.* [8], we were able to investigate the transition from less (slow O^{5+}) to more (swift B^{2+}) perturbative regimes. Last but not least, the choice of Ne and Ar targets also permits the comparison between targets with different number of potentially active electrons, that is, different degrees of complexity. This is particularly important for the electron-capture channel [5] and for both the screening and the antiscreening contributions to the electron-loss process [27].

The paper is organized as follows. In Sec. II, the general aspects of the experimental setup and the procedures to obtain the absolute cross sections are described. In Sec. III, the experimental results for single- and double-electron capture and for single-projectile electron loss are presented and compared to the existent experimental data and to theoretical calculations in the classical Bohr-Lindhard model for the

*gms@vdg.fis.puc-rio.br

single electron capture [28], and in the plane-wave Born approximation [29] and the extended free-collision model [30] for the single electron loss. Also in this section, an analysis of the antiscreening contribution to the single electron loss is made following the reasoning presented by Montenegro *et al.* [27]. Finally, conclusions are drawn in Sec. IV.

II. EXPERIMENT

The B^{2+} and C^{3+} beams with velocities ranging from 1.0 to 4.0 a.u. were obtained from B^- and C^- beams, respectively, provided by the 1.7 MV Pelletron tandem accelerator at the Laboratory of Atomic and Molecular Collisions (Laboratório de Colisões Atômicas e Moleculares—LACAM) of the Federal University of Rio de Janeiro.

The negative ions B^- or C^- are produced by cesium sputtering from a boron-silver or carbon cathode placed at the SNICS (Source of Negative Ions by Cesium Sputtering). They are extracted from the ion source by applying a 5 kV voltage, preaccelerated to a low-energy E_0 of 18.5 keV, and mass selected by a Wien filter before being injected into a 1.7 MV Pelletron tandem accelerator. The ions are, then, attracted to the positively charged central terminal, which is set at a high voltage V and electrostatically focused to the entrance of a gas stripper chamber. The negative ions traverse the stripper cell, where they can either lose none, one, or more electrons, depending on the gas pressure. In the case of the converted B^{2+} or C^{3+} ions, they are again accelerated away from the high-voltage terminal and reach a final kinetic energy (in keV) of $3e \times V + E_0$ for B or $4e \times V + E_0$ for C.

The B^{2+} or C^{3+} ions are selected by an analyzing magnet and directed into the beam line, which is kept at a high vacuum of 10^{-8} Torr. An adjustable four-slit collimator set, 0.65 m downstream from the magnet exit, is used to restrict the beam dimensions to less than the entrance aperture of the gas cell, not only to control the intensity of the main beam, but also to try to reduce impurities in the beam, since it was found that a small proportion of the accelerated beam consists of oxygen ions. Some of these ions collide with the residual gas in the drift region between the accelerator and the analyzing magnet and can be selected by the magnet together with the main beam. A second four-slit collimator set, 2.0 m apart from the first one, is used to reduce the low-energy slit-scattered ions with various charge states and the stray electrons produced in this section of the beam line. Together, both collimating sets define the direction of the ions entering the gas cell; the second set also limits the angular spread of the beam coming from the first adjustable set.

The beam then enters the 12-cm-long differentially pumped target gas cell, which has entrance and exit apertures with diameters of 2.5 and 3.0 mm, respectively, and which are carefully aligned with the two sets of adjustable collimators. The presence of background and distorted beam profiles is due to multiple scattering from the edges of the apertures and is negligible when the beam is strongly collimated and optimized through all apertures. A parallel-plate electrostatic analyzer, located 0.9 m downstream from the second collimator set and consisting of two 5.0-cm-long electrodes 1.5 cm apart, is placed 4.0 cm before the entrance of the target cell. It provides a transverse electric field vertically oriented in respect to the beam line axis, which separates the desired incident charge states—2+ for B and 3+ for C—from spurious components created by collisions of the beam with the residual gas in the beam line before the gas cell.

The pressure in the target cell is measured by an absolute capacitive manometer directly connected to one side of the target chamber. The target gas is supplied through an all-metal ultra fine leak valve. The range of target thickness used is defined by a lower limit imposed by the background in the absence of target gas and an upper limit chosen to guarantee single-collision conditions. In the case of the present measurements, those limits were 0.01 and 0.30 mTorr, respectively, for both targets, with an uncertainty of less than 5%. The absolute calibration of the capacitive manometer is checked by a second pressure gauge connected to the target chamber.

The separation of the different charge states of the beam emerging from the target cell is made by a second electrostatic analyzer, consisting of 16-cm-long parallel electrodes 1.5 cm apart located 10 cm downstream from the cell, and which provides a horizontal transverse analyzing electric field. The electrostatic deflection is chosen so that the fast ions and atoms produced during the collisions are spatially well separated from each other according to their respective charge state. The ions, with up to four different charge states, are simultaneously collected by an *xy*-position-sensitive detector placed 1.75 m downstream from the analyzing parallel-plate electrostatic analyzer. The four ion states correspond to the incident beams (B^{2+} or C^{3+}), the electron loss (B^{3+} or C^{4+}), and the single- and double-electron-capture channels (B^+ and B^0 or C^{2+} and C^+, respectively). The projectile detector consists of a pair of microchannel plates in a chevron configuration with a resistive anode.

The position-sensitive detector allows one to easily spot spurious ions coming together with the main beam. This is specially important for the contamination due to neutral atoms in the beam, which cannot be cleaned by the parallel-plate system upstream from the entrance of the gas cell. This contamination can be observed at the projectile detector in the absence of gas in the target cell and can be discriminated from the main beam by shifting mechanically the position-sensitive detector off the beam line axis. Slit-scattered ions are shown on the position spectra by their greater deflection in the analyzing electrostatic field. The careful collimation procedure used in the present measurements ensures the discrimination of the main and product beams against spurious components.

An image obtained from the position-sensitive detector of the beams which emerge from the target chamber for collisions of 2.0 Mev C^{3+} ions with Ar, after being separated by the second electrostatic analyzer, is shown in Fig. 1. The most intense spot at the center is the main C^{3+} beam; along a horizontal line, one can see at its left the C^{4+} beam from the electron-loss process and at its right the C^{2+} beam from the electron-capture process. At the upper left quadrant of this image, two other spots appear, which are, from right to left, O^{5+} and O^{6+} beams coming from the oxygen contamination from the ion source. The neutral atoms which contaminate the desired charged beams, as mentioned above, do not ap-

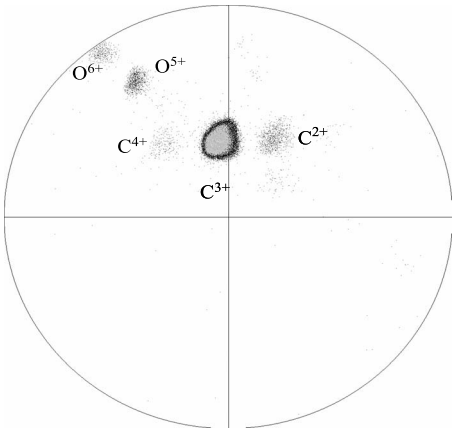

FIG. 1. Image of the emergent beams obtained from the position-sensitive detector for a 2.0 MeV C^{3+} beam impinging on Ar (see text for explanations).

pear in Fig. 1 since this was obtained with the detector already shifted off the beam line axis.

A constant fraction discriminator following the amplifier is set to a level just above the noise so that the smallest pulses from the ions are above the discriminator threshold. Counting rates are kept below 500 counts/s to minimize losses. It was verified that the experimental results are independent of the hit position of the product ions on the detector. It was assumed that the detection efficiency was independent of either the charge state or the energy of the particle hitting the detector, so that the ratio of counting rates is a measure of the ion intensity ratio.

The absolute cross sections were determined using the growth-rate method, which is described in detail by, for example, Tawara and Russek [31] or Santos *et al.* [32]. Briefly, this method consists of measuring the growth rate of the emergent fraction of the incident beam which performs charge-changing collisions as a function of the target thickness, $\pi(P)$, at pressures low enough to ensure the single-collision regime. In order to determine the target thickness, it is necessary to integrate the gas density along the beam path inside the cell. Due to the diffusion of the target gas through the entrance and exit apertures, which separate the gas cell from the high-vacuum up- and down-stream regions, the effective length of the gas target is larger than its geometrical length. Following the suggestion of Toburen and Nakai [33] that the density outside the target cell remains the same as that inside the cell up to a distance equal to the radius of the apertures, falling off as the inverse square of the distance (laminar flow), the target thickness as a function of the target gas pressure is given, in atoms/cm^2, by [31]

$$\pi(P) = \frac{9.62 \times 10^{18} P L_{\text{eff}}}{(273 + T)}, \tag{1}$$

where P is the gas pressure inside the cell in Torr, T is the target temperature in degrees Celsius, and L_{eff} is the effective length of the gas cell in cm, given by [33]

TABLE I. Absolute single electron-capture cross sections (in Mb) for B^{2+} and C^{3+} as a function of the projectile energy, E.

E (MeV)	B^{2+} on Ne	B^{2+} on Ar	C^{3+} on Ar
0.05	1181 ± 88	1761 ± 140	
0.10	1052 ± 78	1636 ± 130	
0.25	879 ± 69	1491 ± 110	1342 ± 110
0.50	505 ± 39	1030 ± 75	1279 ± 92
0.75		660 ± 49	1039 ± 76
1.00	237 ± 20	391 ± 31	742 ± 55
1.50		177 ± 20	471 ± 36
2.00	87 ± 9	76 ± 8	243 ± 19
2.50		40 ± 6	
3.00	36 ± 7	23 ± 4	65 ± 7
3.50		13 ± 3	
4.00	25 ± 5	7.9 ± 1.7	31 ± 4
5.00			11 ± 3

$$L_{\text{eff}} = (L + d_1 + d_2), \tag{2}$$

where L is the geometric length of the target cell and d_1 and d_2 are the diameters of the entrance and exit apertures, respectively. As mentioned above, in our case, the geometrical length of the target cell is 12.0 cm and the apertures diameters are d_1=2.5 mm and d_2=3.0 mm, which gives L_{eff} =12.6 cm.

The cross section σ_{qk} for charge changing in which an incident A^{q+} beam is transformed into an emergent A^{k+} beam, where $k=q+1$ for the loss channel, and $k=q-1$ or $q-2$ for the single- or double-capture channels, respectively, is related to the intensities of the incident and emergent beams by [31,32]

$$\frac{I_k}{I_q} = \sigma_{qk} \pi(P), \tag{3}$$

where I_k is the intensity of the emergent beam after background subtraction and I_q is the intensity of the incident beam. Thus, for each measurement a plot is made of the ratio I_k/I_q as a function of the target pressure and the absolute cross section for the corresponding channel is obtained from the slope of the linear part of this plot. For the present results, the fits were performed taking into account the statistical uncertainties of each measured yield. Thus, the maximum overall statistical and fitting uncertainties were smaller than 20%.

III. RESULTS AND DISCUSSION

Our results for the absolute total cross sections for the single- and double-electron capture and the single electron-loss processes are shown in Tables I–III, respectively.

The single-electron-capture cross sections for B^{2+} from Ne and Ar and C^{3+} from Ar targets from the present measurements are plotted in Figs. 2 and 3, respectively, together with data for C^{3+} and O^{5+} from Melo *et al.* [5] as functions

TABLE II. Absolute double electron-capture cross sections (in Mb) for B^{2+} and C^{3+} as a function of the projectile energy, *E*.

E MeV)	B^{2+} on Ne	B^{2+} on Ar	C^{3+} on Ar
0.05		663 ± 60	
0.10		482 ± 48	
0.25	87 ± 11	254 ± 22	723 ± 62
0.50	40 ± 5	122 ± 11	467 ± 34
0.75		56 ± 6	240 ± 19
1.00	16 ± 3	31 ± 5	122 ± 11
1.50			40 ± 5
2.00			9.6 ± 1.5

of the projectile velocity in atomic units, v/v_0, where v_0 is the Bohr velocity. Also plotted are the data for the single electron capture of B^{2+} by these targets [8] and of C^{3+} by Ar [9] from Dmitriev *et al.* The comparison with the present single-capture data with those published by Dmitriev *et al.* shows a good agreement for the Ar target for both projectiles, except at the lower velocity measured by those authors for C^{3+}, which is about 50% higher than the present results. However, larger discrepancies are observed for the data of B^{2+} on the Ne target. We have no explanation for these so different behaviors; nevertheless, the very good agreement of the present results for C^{3+} with those from Melo *et al.* [5], which were obtained in another laboratory with a completely different setup, gives consistency to these two sets of data.

The data for the different projectiles with Li-like electronic configuration $(1s^2 2s)$—namely B^{2+}, C^{3+} and O^{5+}—present the same general trend as a function of the collision velocity, following the sequence $\sigma_B < \sigma_C < \sigma_O$, as expected from the charge-state dependence of the capture cross sections.

Theoretical calculations for the single electron-capture cross sections of B^{2+} from Ne and Ar and of C^{3+} from Ar were performed using the classical Bohr-Lindhard (B-L) model as presented by Knudsen *et al.* [28]. These results are compared with the present experimental data in Figs. 2 and 4, respectively. In the case of Ar, this comparison is made in a separate figure than that with the other experimental data, in order make the comparison clearer. The agreement between theory and experiment is very good in the case of B^{2+} for both targets, and reasonably good for C^{3+} on Ar, showing that this simple classical model provides good estimates for the single electron capture at the intermediate-velocity regime.

TABLE III. Absolute single electron-loss cross sections (in Mb) for B^{2+} and C^{3+} as a function of the projectile energy, *E*.

E (MeV)	B^{2+} on Ne	B^{2+} on Ar	C^{3+} on Ar
0.25	33 ± 6	14 ± 3	
0.50	68 ± 7	51 ± 5	3.3 ± 0.8
0.75		106 ± 9	9.1 ± 1.7
1.00	145 ± 13	219 ± 19	16 ± 3
1.50		252 ± 25	42 ± 5
2.00	166 ± 15	255 ± 21	75 ± 7
2.50		252 ± 22	
3.00	184 ± 19	262 ± 22	108 ± 10
3.50		248 ± 21	
4.00	182 ± 18	233 ± 20	105 ± 11
5.00			109 ± 12

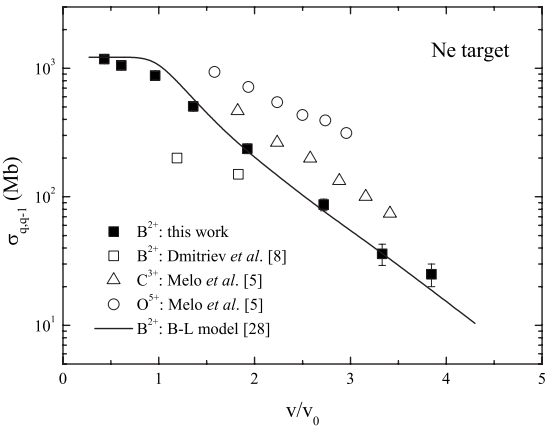

FIG. 2. Absolute single electron-capture cross sections (in Mb) of B^{2+}, C^{3+}, and O^{5+} from Ne as a function of the projectile velocity in atomic units. Experiment: B^{2+} (full squares, this work and open squares, Ref. [8]), C^{3+} (open triangles, Ref. [5]), and O^{5+} (open circles, Ref. [5]). Theory: full line, classical Bohr-Lindhard model for B^{2+} [28].

In Figs. 5 and 6 the present data for the double electron-capture cross sections for B^{2+} from Ne and Ar and C^{3+} from Ar targets, respectively, are shown together with data for C^{3+} and O^{5+} from Melo *et al.* [5]. The data for the double electron capture of B^{2+} by these targets from Dmitriev *et al.* [8] have been also plotted in these figures. Again, a discrepancy of about a factor 5 for the double-capture process occurs for the Ne target. The data from Dmitriev *et al.* for Ar also lie a factor 3 below the present data.

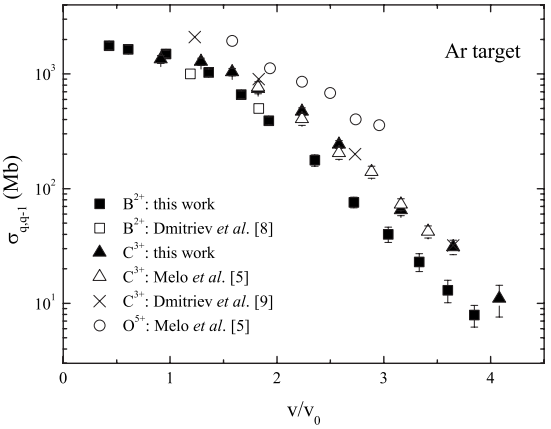

FIG. 3. Absolute single electron-capture cross sections (in Mb) of B^{2+}, C^{3+}, and O^{5+} from Ar as a function of the projectile velocity in atomic units. Experiment: B^{2+} (full squares, this work and open squares, Ref. [8]), C^{3+} (full triangles, this work, open triangles, Ref. [5], and crosses, Ref. [9]), and O^{5+} (open circles, Ref. [5]).

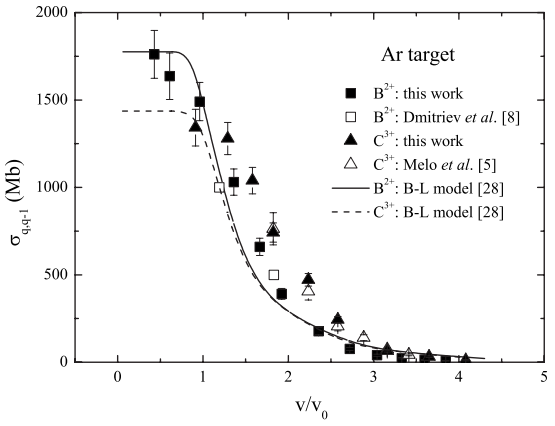

FIG. 4. Experimental and theoretical results for the single electron capture of B^{2+} and C^{3+} from Ar as a function of the projectile velocity in atomic units. Experiment: B^{2+} (full squares, this work and open squares, Ref. [8]); C^{3+} (full triangles, this work and open triangles, Ref. [5]). Theory: classical Bohr-Lindhard model [28]: B^{2+}, full line; C^{3+}, dashed line.

Finally, the single electron-loss cross sections for B^{2+} by Ne and Ar and C^{3+} by Ar targets from the present measurements are plotted in Figs. 7 and 8, respectively, together with data for B^{2+} by these targets [8] and of C^{3+} by Ar [9] from Dmitriev *et al.*, and for C^{3+} and O^{5+} projectiles from Melo *et al.* [5] by the same targets. Again, the present data for the loss of B^{2+}, when compared to the previous data from Dmitriev *et al.* [8], show the same behavior as in the capture process, i. e., a good agreement for Ar, but large discrepancies for Ne. In the case of C^{3+} electron loss by Ar, the results from Dmitriev *et al.* [9] are higher than the present data in the low-velocity region up to a factor 6, tending to agree with them at higher velocities.

Also shown in Figs. 7 and 8 are calculated cross sections for the single electron loss of B^{2+} and C^{3+} by Ne and Ar, respectively. These calculations represent the total single electron-loss cross sections, that is, the sum of the mechanisms which contribute to the single electron loss, namely,

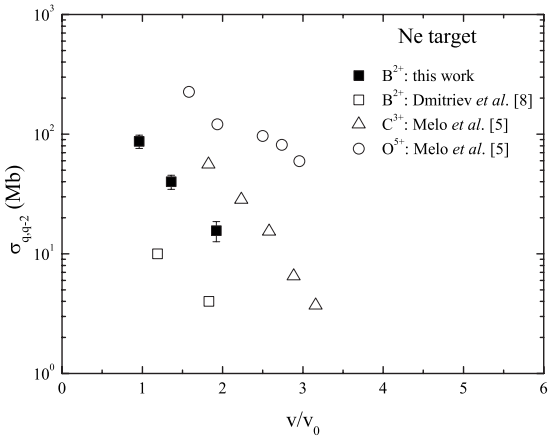

FIG. 5. Absolute double electron-capture cross sections (in Mb) of B^{2+}, C^{3+}, and O^{5+} from Ne as a function of the projectile velocity. Experiment: B^{2+} (full squares, this work and open squares, Ref. [8]), C^{3+} (open triangles, Ref. [5]), and O^{5+} (open circles, Ref. [5]).

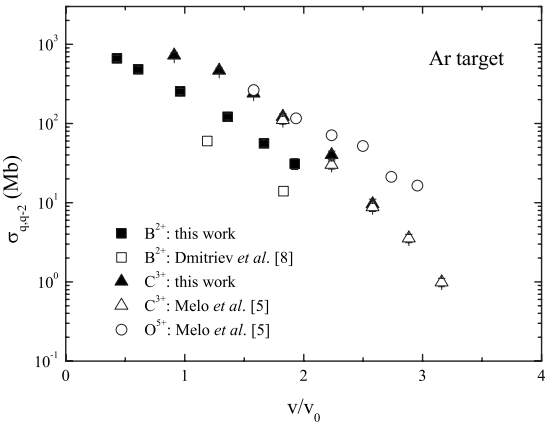

FIG. 6. Absolute double electron-capture cross sections (in Mb) of B^{2+}, C^{3+}, and O^{5+} from Ar as a function of the projectile velocity. Experiment: B^{2+} (full squares, this work and open squares, Ref. [8]), C^{3+} (full triangles, this work and open triangles, Ref. [5]), and O^{5+} (open circles, Ref. [5]).

the screening and antiscreening [34,35]. The screening was calculated using the extended classical-impulse free-collision model as presented by Sigaud [30] and the PWBA, while the antiscreening was obtained from the PWBA extended sum-rule method of Montenegro and Meyerhof [29]. Thus, in these figures the full and dashed lines are the calculated values for B^{2+} and C^{3+}, respectively, using the free-collision model for the screening, and the dotted and dash-dotted lines represent the calculations for B^{2+} and C^{3+}, respectively, using the PWBA for the screening. It can be seen that the calculations using the free-collision model describe the experimental cross sections much better than the PWBA for

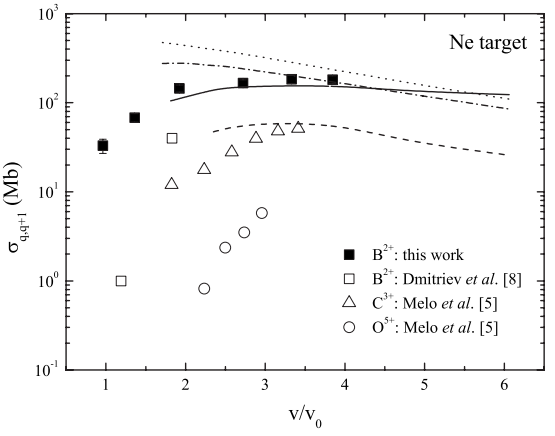

FIG. 7. Absolute single electron-loss cross sections (in Mb) of B^{2+}, C^{3+}, and O^{5+} by Ne as a function of the projectile velocity. Experiment: B^{2+} (full squares, this work and open squares, Ref. [8]), C^{3+} (open triangles, Ref. [5]), and O^{5+} (open circles, Ref. [5]). Theory: full line, sum of screening (extended free-collision model from Ref. [30]) and antiscreening (Ref. [29]) for B^{2+}; dashed line, sum of screening (extended free-collision model from Ref. [30]) and antiscreening (Ref. [29]) for C^{3+}; dotted line, sum of screening and antiscreening in the PWBA (Ref. [29]) for B^{2+}; dash-dotted line, sum of screening and antiscreening in the PWBA (Ref. [29]) for C^{3+} (see text).

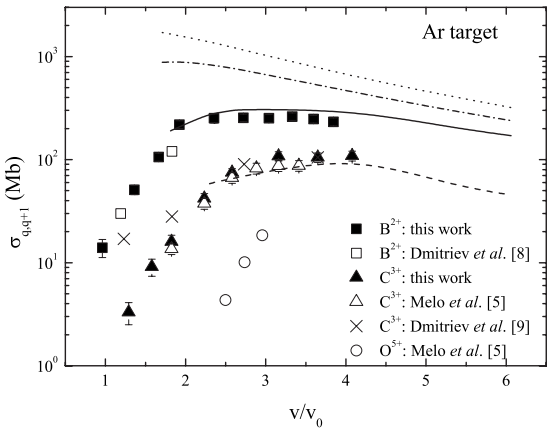

FIG. 8. Absolute total single electron-loss cross sections (in Mb) of B^{2+}, C^{3+}, and O^{5+} by Ar as a function of the projectile velocity. Experiment: B^{2+} (full squares, this work and open squares, Ref. [8]), C^{3+} (full triangles, this work, open triangles, Ref. [5], and crosses, Ref. [9]), and O^{5+} (open circles, Ref. [5]). Theory: full line, sum of screening (extended free-collision model from Ref. [30]) and antiscreening (Ref. [29]) for B^{2+}; and dashed line, sum of screening (extended free-collision model from Ref. [30]) and antiscreening (Ref. [29]) for C^{3+}; dotted line, sum of screening and antiscreening in the PWBA (Ref. [29]) for B^{2+}; dash-dotted line, sum of screening and antiscreening in the PWBA (Ref. [29]) for C^{3+} (see text).

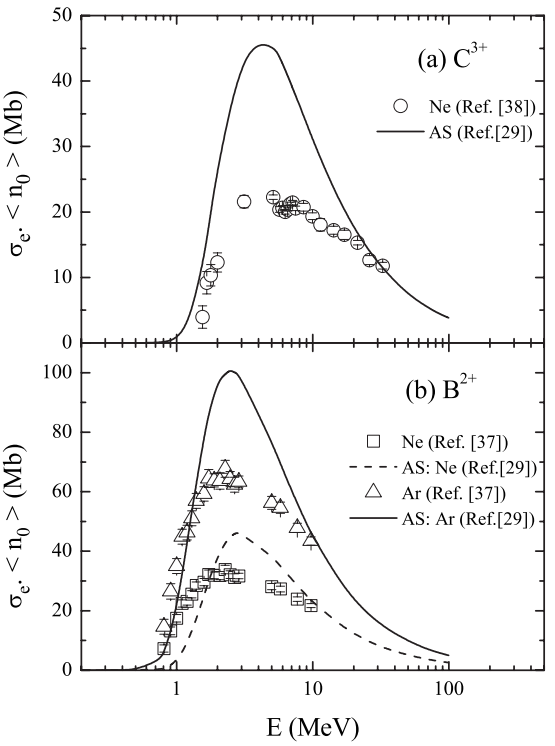

FIG. 9. Comparison of ionization of (a) C^{3+} and (b) B^{2+} ions by electrons and the antiscreening calculations for Ne and Ar targets as a function of the collision energy. Experiment: product of the ionization cross sections of B^{2+} [37] and C^{3+} [38] ions by electrons and the average number of active electrons for the antiscreening for Ne (squares, B^{2+}) and Ar (triangles, B^{2+}, and circles, C^{3+}) from Ref. [27]. Theory: PWBA antiscreening contributions for the electron loss of B^{2+} by Ne (dashed line) and Ar [full line in (b)] and C^{3+} by Ar [full line in (a)] from Ref. [29]. The energies of the electron-impact data are those equivalent to the heavy-ion projectiles with the same velocity (see text).

both projectiles. In the case of the Ar target (Fig. 8), the free-collision model agrees very well with the data for the electron loss of both projectiles. For the Ne target, the calculations using the free-collision model present very good agreement with the experiment only for the B^{2+} projectile; for C^{3+}, the calculations describe the data fairly well only in the high-velocity regime, overestimating the experiment for velocities below 3 a.u. Even so, it should be mentioned that the modifications introduced in Ref. [30] in respect to the first version of the model, which appears in Melo *et al.* [5], show a remarkable improvement, as can be seen if one compares, for example, the present Fig. 8 with Fig. 3 of Ref. [5]. It should also be stressed at this point that the calculations for the screening using the free-collision model are limited to projectile velocities larger than the orbital velocity of the projectile active electron, which is 1.7 a.u. and 2.2 a.u. for B^{2+} and C^{3+}, respectively [30]. Due to this constraint, the calculations performed with this model do not cover the whole region of velocities of the present measurements.

The good agreement of the calculated total electron-loss cross sections using the free-collision model for the screening contribution with the present data for both B^{2+} and C^{3+} ions, as well as the previous results from Ref. [30] using this model in the calculations of total and partial electron-loss cross sections of anions by noble gases below the antiscreening threshold, led us to analyze in more detail the calculations for the antiscreening contribution, even though we have not measured this contribution separately. This has been done following the reasoning presented by Montenegro *et al.* for the electron loss of He^+ ions by noble gases [27]. Here we have assumed that the target electrons, which are active in the projectile ionization, act independently from each other, that is, within the independent-particle model, and have taken as the average number of active target electrons, $\langle n_0 \rangle$, those found by Montenegro *et al.* for He^+ projectiles, namely, 4.3 and 8.6 for Ne and Ar, respectively. The latter assumption was based on the fact that the ionization energies of the B^{2+} and C^{3+} ions −37.9 and 64.5 eV, respectively [36]—are not very different than that of the He^+ ion (54.5 eV). Thus, we have plotted in Fig. 9 the product of the ionization cross sections of B^{2+} [37] and C^{3+} [38] ions by electrons from Crandall *et al.*, σ_e, by $\langle n_0 \rangle$, together with the PWBA-based calculations for the antiscreening contribution for the present collision systems as a function of the projectile energy. In the case of the electron-impact data, the collision energies are those equivalent to the heavy-ion projectiles with the same velocity. First of all, it can be seen that the antiscreening calculations tend to agree with the product $\sigma_e \langle n_0 \rangle$ at high energies, thus, presenting the same asymptotic behavior previously observed for the He^+ projectile [27]. Since, for this projectile, the number of potentially active target electrons for Ne and Ar varies very slowly with the projectile energy [27], the assumption used here that $\langle n_0 \rangle$ is independent of the projectile ion seems to be reasonable for the present projectiles, at least for few-electrons ions with similar ionization energies.

In the case of the Ne target, the quite good agreement observed in Fig. 9 for B^{2+} is not surprising since the results for C^{3+} projectiles on Ne reported by Kirchner *et al.* [7] show a good agreement between the PWBA calculations for the antiscreening and a more sophisticated model for the loss-ionization process. For Ar, the present calculations describe fairly well the product $\sigma_e\langle n_0\rangle$ in the low-energy region, near the ionization threshold, for both projectiles, although the model is not quite well suited at this region. Actually, the lower limit of validity of the free-collision model calculations for the screening contribution also lies around the threshold for the antiscreening. The present measurements are in a region which begins below the threshold of the antiscreening and goes beyond its maximum. Near the maximum, there are discrepancies between the antiscreening calculations and the product $\sigma_e\langle n_0\rangle$, which can reach a factor 2, as can be seen in Fig. 9. Thus, the fact that an overall good agreement between the present calculations and the measured data for the total electron-loss cross sections has been observed can only be better understood with exclusive measurements in which both the screening and the antiscreening contributions are separately determined. This can be accomplished in experiments where the emergent charge states of the projectile are measured in coincidence with the charge states of the recoil ions produced in the collision, as was done, for example, by Montenegro *et al.* for the electron loss of He^+ ions by noble gases [27].

IV. CONCLUSIONS

We have measured absolute cross sections for the total projectile single electron loss and single and double electron capture of B^{2+} ions colliding with Ne and Ar targets, and C^{3+} ions colliding with Ar targets, in the energy range from 0.1 to 4.0 MeV. On the one hand, the present data for B^{2+} have been compared with the only data available in the literature for the same targets and in the same velocity range, namely, those from Dmitriev *et al.* [8]. There is a good agreement between the two sets of data for the single-electron loss and single-electron capture for the Ar target, but the present data lie, in general, well above the older set for these two processes in the case of the Ne target, and for the double electron capture for both targets. On the other hand, the comparison of the present data for the C^{3+} projectile with previous data reported by Melo *et al.* [5] shows a very good agreement over the whole velocity region where both data sets overlap, for all the processes studied here.

Calculations have been performed for the single electron capture of B^{2+} from Ne and Ar and of C^{3+} from Ar using the classical Bohr-Lindhard model from Knudsen *et al.* [28], presenting a very good overall agreement. For the electron loss of B^{2+} and C^{3+} by Ne and Ar, the calculations for the screening contribution have been made using two different models—the classical-impulse free-collision model in the extended version of Ref. [30] and the PWBA, while the antiscreening contribution have been evaluated using the PWBA extended sum-rule method of Montenegro and Meyerhof [29]. The theoretical calculations which have used the extended free-collision model for the screening mode describe the experimental data very well for both projectiles and targets above the limit of validity of the model, while the PWBA calculations overestimate the data for the whole range of velocities of the present work.

We have analyzed the present calculations for the antiscreening contribution in a way similar to that presented by Montenegro *et al.* for the electron loss of He^+ ions by noble gases [27], within the independent-particle model. The antiscreening calculations have been compared to the experimental cross sections for the ionization of B^{2+} and C^{3+} ions by electrons multiplied by an average number of active electrons for the Ne and Ar targets. At the asymptotic high-energy region the agreement was quite good; however, discrepancies have been observed in the region around the maximum of the antiscreening contribution, which is the region where the present measurements lie. These discrepancies can only be better clarified if coincidence measurements of exclusive cross sections are performed, in order to separate experimentally the contributions from the screening and the antiscreening. Thus, the theoretical models used here can be more effectively tested with a direct comparison with the experiment.

ACKNOWLEDGMENTS

This work was supported in part by the Brazilian agencies CNPq and FAPERJ.

[1] A. K. Kaminskii and A. A. Vasilev, Phys. Part. Nucl. **29**, 201 (1998).
[2] J. S. Yoon and Y. D. Jung, Phys. Plasmas **6**, 3391 (1999).
[3] R. D. DuBois *et al.*, Phys. Rev. A **68**, 042701 (2003).
[4] R. D. DuBois *et al.*, Phys. Rev. A **70**, 032712 (2004).
[5] W. S. Melo, M. M. Sant'Anna, A. C. F. Santos, G. M. Sigaud, and E. C. Montenegro, Phys. Rev. A **60**, 1124 (1999).
[6] T. Kirchner, M. Horbatsch, and H. J. Lüdde, J. Phys. B **37**, 2379 (2004).
[7] T. Kirchner, A. C. F. Santos, H. Luna, M. M. Sant'Anna, W. S. Melo, G. M. Sigaud, and E. C. Montenegro, Phys. Rev. A **72**, 012707 (2005).
[8] I. S. Dmitriev, Ya. A. Teplova, and Yu. A. Fainberg, Zh. Eksp. Teor. Fiz. **116**, 1538 (1999) [Sov. Phys. JETP **89**, 830 (1999)].
[9] I. S. Dmitriev, Ya. A. Teplova, Yu. A. Belkova, and N. V. Novikov, J. Surf. Invest. **2**, 270 (2008)
[10] R. Janev, Phys. Scr. **T62**, 5 (1996).
[11] R. Hippler, S. Datz, P. D. Miller, P. L. Pepmiller, and P. F. Dittner, Phys. Rev. A **35**, 585 (1987).
[12] W. Fritsch and C. D. Lin, Phys. Rev. A **45**, 6411 (1992).
[13] P. S. Krstić, D. Schultz, and G. Bent, Phys. Scr. **T62**, 21 (1996).
[14] L. F. Errea, J. D. Gorfinkel, C. Harel, H. Jouin, A. Macías, L. Méndez, B. Pons, and A. Riera, Phys. Scr. **T62**, 27 (1996);

T62, 33 (1996).
[15] N. Shimakura, S. Suzuki, Y. Murakami, J. P. Gu, G. Hirsch, R. J. Buenker, M. Kimura, and I. Shimamura, Phys. Scr. **T62**, 39 (1996).
[16] R. Janev, E. A. Solov'ev, and G. Ivanovski, Phys. Scr. **T62**, 43 (1996).
[17] M. Garguad and R. McCarroll, Phys. Scr. **T62**, 49 (1996).
[18] J. P. Hansen and A. Dubois, Phys. Scr. **T62**, 55 (1996).
[19] W. Fritsch, Phys. Scr. **T62**, 59 (1996).
[20] Y. D. Wang, N. Toshima, and C. D. Lin, Phys. Scr. **T62**, 63 (1996).
[21] D. Schultz, P. S. Krstić, and C. O. Reinhold, Phys. Scr. **T62**, 69 (1996).
[22] H. F. Busnengo, S. E. Corchs, A. E. Martínez, and R. D. Rivarola, Phys. Scr. **T62**, 88 (1996).
[23] M. Das, M. Purkait, and C. R. Mandal, Phys. Rev. A **57**, 3573 (1998); J. Phys. B: At., Mol. Opt. Phys. **31**, 4387 (1998).
[24] M. C. Bacchus-Montabonel, Phys. Rev. A **59**, 3569 (1999).
[25] M. Purkait, S. Sounda, A. Dhara, and C. R. Mandal, Phys. Rev. A **74**, 042723 (2006).
[26] S. Ghosh, A. Dhara, C. R. Mandal, and M. Purkait, Phys. Rev. A **78**, 042708 (2008).
[27] E. C. Montenegro, A. C. F. Santos, W. S. Melo, M. M. Sant'Anna, and G. M. Sigaud, Phys. Rev. Lett. **88**, 013201 (2001).
[28] H. Knudsen, H. K. Haugen, and P. Hvelplund, Phys. Rev. A **23**, 597 (1981).
[29] E. C. Montenegro and W. E. Meyerhof, Phys. Rev. A **43**, 2289 (1991).
[30] G. M. Sigaud, J. Phys. B **41**, 015205 (2008).
[31] H. Tawara and A. Russek, Rev. Mod. Phys. **45**, 178 (1973).
[32] A. C. F. Santos, W. S. Melo, M. M. Sant'Anna, G. M. Sigaud, and E. C. Montenegro, Rev. Sci. Instrum. **73**, 2369 (2002).
[33] L. H. Toburen and M. Y. Nakai, Phys. Rev. **177**, 191 (1969).
[34] J. H. McGuire, N. Stolterfoht, and P. R. Simony, Phys. Rev. A **24**, 97 (1981).
[35] E. C. Montenegro, W. E. Meyerhof, and J. H. McGuire, Adv. At., Mol., Opt. Phys. **34**, 249 (1994).
[36] T. A. Carlson, C. W. Nestor, Jr., N. Wasserman, and J. D. McDowell, At. Data **2**, 63 (1970).
[37] D. H. Crandall, R. A. Phaneuf, D. C. Gregory, A. M. Howald, D. W. Mueller, T. J. Morgan, G. H. Dunn, D. C. Griffin, and R. J. W. Henry, Phys. Rev. A **34**, 1757 (1986).
[38] D. H. Crandall, R. A. Phaneuf, B. E. Hasselquist, and D. C. Gregory, J. Phys. B **12**, L249 (1979).